ACS APPLIED MATERIALS & INTERFACES

Research Article

Cite This: ACS Appl. Mater. Interfaces 2018, 10, 18869−18878

www.acsami.org

Pick a Color MARIA: Adaptive Sampling Enables the Rapid Identification of Complex Perovskite Nanocrystal Compositions with Defined Emission Characteristics

Leonard Bezinge,[†] Richard M. Maceiczyk,[†] Ioannis Lignos,[†] Maksym V. Kovalenko,[*,‡,§] and Andrew J. deMello[*,†]

[†]Institute for Chemical and Bioengineering, Department of Chemistry and Applied Biosciences and [‡]Institute of Inorganic Chemistry, Department of Chemistry and Applied Biosciences, ETH Zürich, Vladimir-Prelog-Weg 1, 8093 Zürich, Switzerland

[§]Laboratory for Thin Films and Photovoltaics, Empa—Swiss Federal Laboratories for Materials Science and Technology, Überlandstrasse 129, 8600 Dübendorf, Switzerland

Supporting Information

ABSTRACT: Recent advances in the development of hybrid organic−inorganic lead halide perovskite (LHP) nanocrystals (NCs) have demonstrated their versatility and potential application in photovoltaics and as light sources through compositional tuning of optical properties. That said, due to their compositional complexity, the targeted synthesis of mixed-cation and/or mixed-halide LHP NCs still represents an immense challenge for traditional batch-scale chemistry. To address this limitation, we herein report the integration of a high-throughput segmented-flow microfluidic reactor and a self-optimizing algorithm for the synthesis of NCs with defined emission properties. The algorithm, named Multiparametric Automated Regression Kriging Interpolation and Adaptive Sampling (MARIA), iteratively computes optimal sampling points at each stage of an experimental sequence to reach a target emission peak wavelength based on spectroscopic measurements. We demonstrate the efficacy of the method through the synthesis of multinary LHP NCs, $(Cs/FA)Pb(I/Br)_3$ (FA = formamidinium) and $(Rb/Cs/FA)Pb(I/Br)_3$ NCs, using MARIA to rapidly identify reagent concentrations that yield user-defined photoluminescence peak wavelengths in the green−red spectral region. The procedure returns a robust model around a target output in far fewer measurements than systematic screening of parametric space and additionally enables the prediction of other spectral properties, such as, full-width at half-maximum and intensity, for conditions yielding NCs with similar emission peak wavelength.

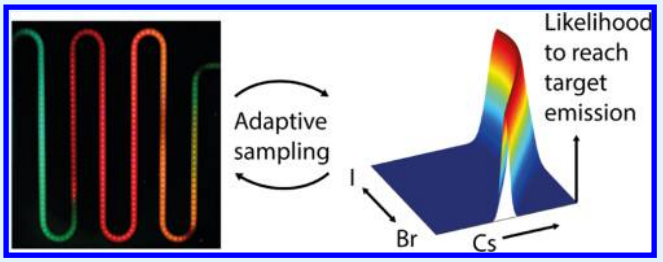

KEYWORDS: *perovskites, quantum dots, nanocrystals, microfluidics, Kriging, optimization*

INTRODUCTION

Lead halide perovskite (LHP) nanocrystals (NCs), first reported just a few years ago,[1,2] are an important class of colloidal semiconductor NCs with attractive optoelectronic properties[3−5] and potential applications in lasers,[6−9] light-emitting devices (LEDs),[10−14] fast single-photon sources,[15,16] or as photosensitizers or absorbers in photovoltaic cells[17−20] and photodetectors.[21] LHPs, with the general formula $APbX_3$, consist of an organic or inorganic A-site cation (commonly methylammonium (MA^+), formamidinium (FA^+), cesium (Cs^+), or a mixture thereof) residing within a 12-fold coordinated site formed by $[PbX_6]$ octahedra, where X is Cl^-, Br^-, I^-, or a mixture thereof. The ability of hybrid LHP materials to form solid solutions of mixed cations and anions within a single homogeneous phase enables broad compositional tuning of optical properties. A large variety of LHP nanocrystal compositions have been reported and include, but are not limited to, $MAPbX_3$,[1,10,22] $FAPbX_3$,[23−27] $CsPbX_3$,[2,28−30] doped $CsPbX_3$ (Mn^{2+}, Sn^{2+}, Cd^{2+}, Zn^{2+}, or Bi^{3+} as dopant),[31−35] and $(Cs/FA)PbI_3$ NCs.[25] An increase in compositional complexity is often motivated by a desire to improve performance and mitigate stability issues, which remain the primary challenge hindering the implementation of LHPs in next-generation solar cells and other optoelectronic devices. In this respect, the introduction of mixed cations or interstitial defects thermodynamically stabilizes the photoactive phase[36] and even decreases the sensitivity of LHPs to light, moisture, and temperature.[37−39] Such multinary LHPs, in the form of thin films, have been the subject of intense investigation for application in solar cells, with materials such as $(Cs/MA/FA)Pb(Br/I)_3$ and $(Rb/Cs/MA/FA)PbI_3$ demonstrating remarkable photoconversion efficiencies (above 20%) over timespans of several weeks.[37,38]

Computer simulations and empirical theories (such as the Goldschmidt tolerance factor[40,41]) have also been used to evaluate the feasibility and consequences of introducing various

Received: February 28, 2018
Accepted: May 16, 2018
Published: May 16, 2018

DOI: 10.1021/acsami.8b03381
ACS Appl. Mater. Interfaces 2018, 10, 18869−18878

cations into the LHP crystal lattice and confirm the empirical observation that complex, multinary perovskites are often superior to simpler compositions.[25,42,43] The synthesis of perovskite NC populations with defined and homogeneous composition, size, and dimensionality is enormously challenging because these properties are highly sensitive to synthetic conditions such as the type and concentration of both precursors and surfactants.[24,27,44] Understanding of the formation mechanism of LHP NCs is limited by practical hurdles in controlling an in situ monitoring of these reactions due to short reaction times (on the order of a few seconds) and fast ion exchange kinetics, even at room temperature (RT).[25,26,28] Indeed, in the case of complex LHPs, empiric synthesis optimization requires a very large number of experiments, inaccessible with the flask-based syntheses. In such an endeavor, segmented-flow microfluidic reactors, equipped with real-time optical detectors, can tremendously accelerate the parametric screening, while consuming miniscule amounts of reagents.[26−28,45−53] That said, for the multidimensional parameter spaces encountered in LHP systems, the complete mapping of parameter space with incremental changes in all experimental parameters and containing all parameter combinations is still unfeasible and thus a more intelligent, target-oriented approach/algorithm would strongly benefit the exploration of novel and compositionally complex NCs.[54−57]

In the context of LHPs, the primary defining characteristic of interest is the emission peak wavelength. Herein, we use a Kriging-based algorithm to target a specific photoluminescence (PL) emission wavelength and find all possible experimental conditions yielding NCs with the desired emission, initially neglecting other spectral properties. For a given class of complex LHP NCs, similar PL peak wavelengths might originate from a multitude of combinations of compositions, sizes, or even NC shapes, with two latest parameters influencing the emission energy by quantum-size effects. However, these various NCs, although exhibiting same PL peak wavelengths, might exhibit vastly different PL quantum yield (PL QY), PL emission line width, and, particularly important for LHP NCs, stability. The selection of promising material candidates for performance tests and offline characterization relies on the identification of trends and patterns in the functional dependence of the spectral properties. Initially developed for geological applications in the 1960s, Kriging metamodels have been extensively used in noisy computer simulations, engineering design problems, and more recently as a prediction tool for the reaction outcomes of photoluminescent nanomaterials.[51,58,59] They define a family of nonparametric interpolation methods used in global optimization problems[60−62] and provide an attractive platform for the rapid exploration of complex parameter space compared with rigorous physical models used in thorough optimizations of industrial chemical processes.[63]

In the current work, we present an efficient goal-seeking algorithm named Multiparametric Automated Regression Kriging Interpolation and Adaptive Sampling (MARIA), which identifies future reaction conditions based on previous measurements. In conjunction with a microfluidic reactor, MARIA forms a self-optimizing system that autonomously explores conditions of interest. The primary goal of the developed platform is to rapidly return an accurate model identifying reaction conditions that yield NCs with desired optical properties. We demonstrate the efficacy of our method for the synthesis of $(Cs/FA)Pb(Br/I)_3$ NCs with controlled PL emission maxima at either 560, 620, or 680 nm. We further test the accuracy of the resulting model for 680 nm emitting NCs and compare the synthesized NCs in terms of full width at half-maximum (FWHM) and PL intensity. Finally, we extend the optimization to three-dimensional parameter space for the synthesis of complex $(Rb/Cs/FA)Pb(Br/I)_3$ NCs with PL peak at 600 nm. This work will guide future experimental efforts on a large scale (typical reaction flasks), by suggesting a set of synthesis protocols for designated emission ranges. Once these syntheses will be adapted by the batch reactors, the obtained NCs will be compared in terms of their stability and durability.

■ ADAPTIVE SAMPLING ALGORITHM

MARIA provides a response surface from data observed at previously sampled points within a parameter space as well as a method to select the next point to be sampled. We choose Kriging as basis for MARIA because it has already been introduced in the context of complex reaction systems and other black-box systems.[51,60] It is well-suited as a response surface model for complex, unknown systems as it does not require any assumptions about the functional dependence of output parameters on experimental conditions. In the case of single-output systems, Kriging is preferred to neural networks as it is more easily trained while requiring fewer data.[64] Moreover, in addition to a predictor value, Kriging supplies the variance corresponding to each prediction, which can subsequently serve as a tool to guide sampling. Commonly, a two-step approach is adopted in global optimization problems,[62] with Kriging predictors being first computed throughout the parameter space and then the probability of improving the current minimum being evaluated to determine the optimal sampling position. Kriging-based goal-seeking methods, in contrast, have received very little attention.[61] Herein, we propose a one-step approach that directly assesses the likelihood that any experimental condition will yield a predefined target wavelength. The MARIA and adaptive sampling procedure strategy is illustrated in Figure 1: starting from an initial set of measurements, the adaptive sampling algorithm fits a Kriging model and computes optimal parameters for subsequent sampling with the highest likelihood of reaching a user-defined target value. The process is repeated until the end criterion is met (or in our case, a predefined number of iterations).

We note that in the following we use bold lowercase letters for (column) vectors (with the unit vector denoted $\mathbf{1}$) and bold uppercase letters for matrices ($\mathbf{I}$ being the identity matrix). Superscript T indicates the transpose of a vector/matrix. Regular font symbols and letters refer to scalar functions, variables, or constants. A basic assumption of Kriging is that observables y at positions $\mathbf{x}$ within the parameter space are realizations of a stochastic process Y comprising a model constant β and local deviations $Z(\mathbf{x})$[60,65]

$$Y(\mathbf{x}) = \beta + Z(\mathbf{x}) \tag{1}$$

In addition, we postulate that two stochastic variables $Y(\mathbf{x}_i)$ and $Y(\mathbf{x}_j)$ at positions $\mathbf{x}_i$ and $\mathbf{x}_j$ in a d-dimensional parameter space are correlated and their degree of correlation is quantified by the function $\mathrm{Corr}(Y(\mathbf{x}_i), Y(\mathbf{x}_j))$, which depends on the weighted "distance" between the two positions according to[60]

DOI: 10.1021/acsami.8b03381
ACS Appl. Mater. Interfaces 2018, 10, 18869−18878

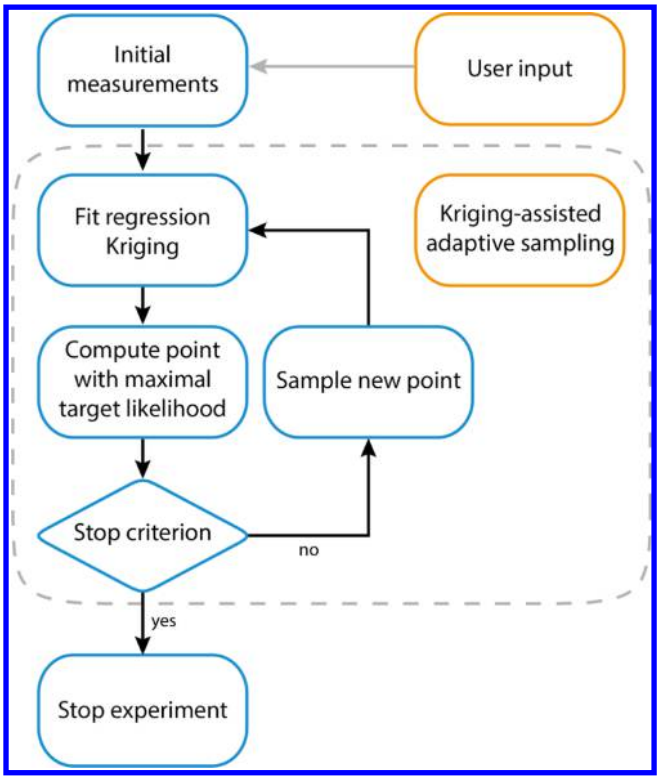

Figure 1. Flowchart describing the Kriging-based adaptive sampling procedure (MARIA). The process is fully automated, and user influence is limited to the choice of a set of initial sampling points.

$$\mathrm{Corr}(Y(\mathbf{x}_i), Y(\mathbf{x}_j)) = \exp\left(-\sum_{d}^{l=1} \theta_l |x_i - x_j|^{p_l}\right) \quad (2)$$

The exponents p_l are an expression of the smoothness of the data, with $p_l = 2$ corresponding to a smooth and continuous response surface, as is expected for our system. In fact, the choice of $p_l = 2$ results in a model based on a Gaussian kernel with variance $1/\theta_l$.[59] The coefficients θ_l determine how rapidly the correlation between two variables decreases with distance in each dimension, which can be seen as a measure of dimensional activity. Inactive dimensions (those with rapidly decreasing correlation) have high values of θ_l, whereas active dimensions require small values of θ_l to capture the long-range correlation of function values.[60] To generate a model from these assumptions, Kriging involves the search of a random process that best-describes a set of n measured samples, $\mathbf{y} = [y(\mathbf{x}_1), ..., y(\mathbf{x}_n)]^T$.[58] Following the classical derivation of Kriging, we consider a vector of random variables $\mathbf{Y} = [Y(\mathbf{x}_1), ..., Y(\mathbf{x}_n)]^T$ at sampled positions $\mathbf{x}_1, \mathbf{x}_2, ..., \mathbf{x}_n$, with a mean $\mathbf{1}\mu$ and a covariance matrix $\mathrm{Cov}(\mathbf{Y}) = \sigma^2\mathbf{R}$, where σ is the standard deviation and $\mathbf{R}$ is the correlation matrix with elements $R_{ij} = \mathrm{Corr}(Y(\mathbf{x}_i), Y(\mathbf{x}_j))$.[65] This definition of covariance implies that a variable is perfectly correlated with itself according to 2 ($R_{ii} = 1$), which forces the response surface to include measured values without considering noise or experimental error. In the context of nanomaterial synthesis, we expect that the optical properties of NC populations will be subject to noise emanating from limited measurement precision and reaction control. To incorporate this into the model, we allow regression of experimental data by adding a regression parameter Λ to the diagonal element of the correlation matrix R_{ij}, thus giving rise to a new covariance matrix $\mathrm{Cov}'(\mathbf{Y}) = \sigma^2(\mathbf{R} + \Lambda\mathbf{I})$.[59] An optimal model constitutes a combination of parameters θ_i and Λ constructing a stochastic process that most likely describes the measured data. To estimate the value of observables at an arbitrary point $\mathbf{x}^*$, we seek to obtain a predictor $\hat{y}(\mathbf{x}^*)$ quantifying the functional dependence of the output value on the reaction conditions. We accomplish this by maximizing the likelihood to generate the set of observables $\mathbf{y}$ from the stochastic process previously described to obtain the so-called best linear unbiased predictor (BLUP) $\hat{y}(\mathbf{x}^*)$ and its associated variance $\hat{s}^2(\mathbf{x}^*)$ (derivation provided in the Supporting Information)[65]

$$\hat{y}(\mathbf{x}^*) = \hat{\mu} + \mathbf{r}(\mathbf{x}^*)^T(\mathbf{R} + \Lambda\mathbf{I})^{-1}(\mathbf{y} - \mathbf{1}\hat{\mu}) \quad (3)$$

The correlation vector $\mathbf{r}(\mathbf{x}^*)$, with elements given by $r_i(\mathbf{x}^*) = \mathrm{Corr}(Y(\mathbf{x}^*), Y(\mathbf{x}_i))$, quantifies the correlation of an arbitrary point with the measured data points and essentially corresponds to the radial basis function of the metamodel.

Figure 2a shows the effect of parameter θ on the function predictor and the calculated model likelihood for $\Lambda = 0$. High values of θ result in a predictor that is weakly influenced by the data with localized deviations from the model mean $\hat{\mu}$. In contrast, for low values of θ, predictor values are highly correlated to the data over long distances. There exists an optimal value of θ for which the correlation function most likely describes the measured values, which MARIA automatically chooses. If we consider a system subject to noise or experimental error, the case $\Lambda = 0$ returns a distorted response surface as it is forced to go through every sample point ($\hat{s}(\mathbf{x}_i) = 0$). In contrast, regressing the data ($\Lambda > 0$) better captures the shape of the underlying function (Figure 2b). MARIA returns a response surface (with parameters θ and Λ) that maximizes the likelihood of generating the observables. This combination of parameters is inherent to the measured data and independent of the location at which a prediction is made.

The next step in building the optimization algorithm is to determine a way to select subsequent points for sampling. Recalling that Kriging models assume that observables are realizations of a stochastic process immediately enables us to statistically evaluate predictions. Outputs of the BLUP at reaction conditions $\mathbf{x}^*$ correspond to a probability density function (PDF) of a Gaussian distribution, with mean $\hat{y}(\mathbf{x}^*)$ and variance $\hat{s}^2(\mathbf{x}^*)$.[60] Integrating the PDF returns the probability of measuring an observable at point $\mathbf{x}^*$ within the range of integration. By calculating the probability to improving the current minimum, $P(y < y_{\min})$, at every coordinate, this feature can be used directly in global optimization problems, where the goal is minimization of an objective function (Figure 2c).[61] In the case of a goal-seeking problem, the system is commonly transformed into an optimization problem by transformation of the objective function, e.g., minimize $(y - y^*)^2 + v$ for a target value of y^* with minimal secondary property v (e.g., FWHM, inverse of intensity).[55] However, two concerns arise from this approach. First, it is up to the user to determine the weights of each property in the objective function, which is arbitrary and might vary depending on the materials and their applications.[66] Second, these algorithms return a single optimal point. However, if a nanomaterial is unstable or difficult to use for device fabrication, the optimization will fall short and the user must redefine boundaries that exclude the current material and allow identification of a new candidate. For LHPs, material stability has been the primary hurdle in the development of new materials and has been shown to be strongly dependent on

DOI: 10.1021/acsami.8b03381
ACS Appl. Mater. Interfaces 2018, 10, 18869−18878

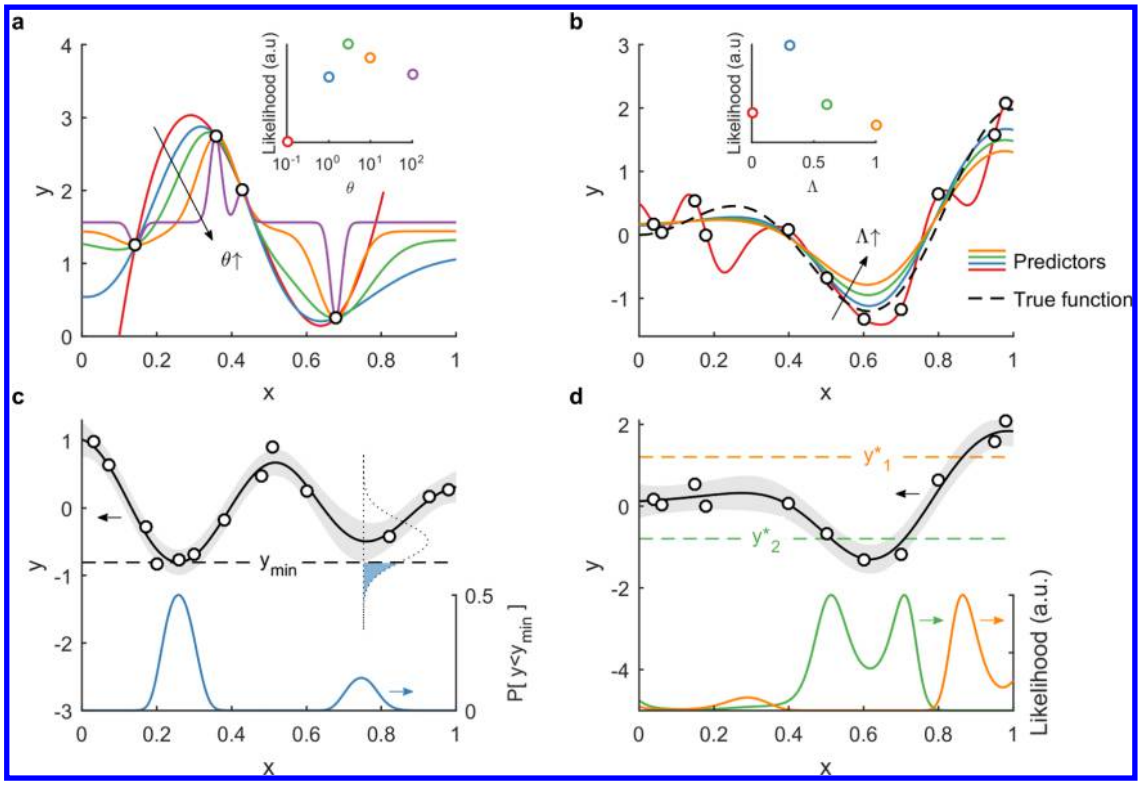

Figure 2. (a) Influence of θ on Kriging predictors applied to a set of four arbitrary data points with values 10^{-1}, 1, 3, 10, and 100. The inset shows the calculated likelihood for each predictor. MARIA automatically chooses the predictor corresponding to the maximal likelihood. (b) Influence of the regression parameter, Λ, on Kriging predictors. Data points are generated by adding noise to an arbitrary function (dashed line). Starting from $\Lambda = 0$ (pure interpolation), larger values of Λ imply larger sampling errors. The inset shows the calculated likelihood of the predictors for increasing Λ. (c) Optimization approach: probability, P, to improving current predicted minimum y_{min} (blue curve). The probability is calculated by integrating the probability density function (PDF) (dotted curve, shown for $x = 0.75$) with the mean given by the predictor (solid line) and variance (gray area) returned by Kriging. (d) Goal-seeking approach implemented by MARIA: likelihoods of the predictions to reach two different target values y_1^* and y_2^*. This one-step method calculates the likelihood directly from Kriging parameters θ and Λ, without necessarily evaluating the predictor.

both composition and doping.[37,38,67] In this respect, a target-oriented approach returning all conditions that yield the desired emission is preferable and eventually provides a basis for comparing optical properties (e.g., FWHM, intensity) of materials with similar emission maximum. Jones et al.[61] describe a Kriging-based target-oriented approach by adding an hypothetical data point at position $\mathbf{x}^*$ with value y^* (target output) to the set of observables. In a subsequent step, parameters θ_l and Λ are computed via the maximum likelihood evaluation and the resulting likelihood measures the credibility of the hypothesis. This procedure repeats at every point of interest before selecting the point with the highest credibility, rendering this approach computationally intensive and impractical for high-dimensionality systems. To address this limitation, we propose a streamlined approach, where first, coefficients θ_l and Λ are optimized using previously sampled data. The algorithm then computes the likelihood of any position $\mathbf{x}^*$ resulting in the targeted value y^* under the hypothesis that $\hat{y}(\mathbf{x}^*) = y^*$. To illustrate this concept, Figure 1d displays the likelihood of a Kriging model reaching two different target values y_1^* and y_2^*. The next measurement condition is chosen at the point with the highest likelihood. Our approach exhibits several key advantages: first, it is a one-step approach and does not require the computation of the full response surface at each iteration (likelihood estimation requires only parameters θ_l and Λ, without computing a BLUP), considerably speeding up computation times, especially for high-dimensionality systems. Second, no transformation of the system through an objective function is needed, which renders the analysis of outputs and comparison to experimental data simpler and more intuitive.

Concerning the numerical implementation of the algorithm, the parameter space is discretized in a fine grid, i.e., with the smallest physically meaningful and experimentally feasible spacing between neighboring parameter combinations. Each discrete position corresponds to a specific experimental condition and thus a purposeful grid spacing will reflect the limited accuracy of the experimental setup. The interpolated values and likelihood of reaching the target are evaluated at every point of the grid. In the case of a high-dimensional system, a rougher discrete grid might be preferable to speed up the computation of the algorithm at the expense of the model fidelity.

The quality of the final model is assessed by "leave-one-out" cross-validation, which evaluates the sensitivity of the model to lost information. The standardized cross-validated residuals, E_i, are given by[60]

$$E_i = \frac{y_i(\mathbf{x}_i) - \hat{y}_{-i}(\mathbf{x}_i)}{\hat{s}_{-i}(\mathbf{x}_i)} \tag{4}$$

Here, $y_i(\mathbf{x}_i)$ is the measured value at position $\mathbf{x}_i$ and $\hat{y}_{-i}(\mathbf{x}_i)$ and $\hat{s}_{-i}(\mathbf{x}_i)$ are Kriging predictions obtained after removing the i-th measurement point. First and second moments Q_1 and Q_2 of the standardized residuals provide valuable information about

DOI: 10.1021/acsami.8b03381
ACS Appl. Mater. Interfaces 2018, 10, 18869−18878

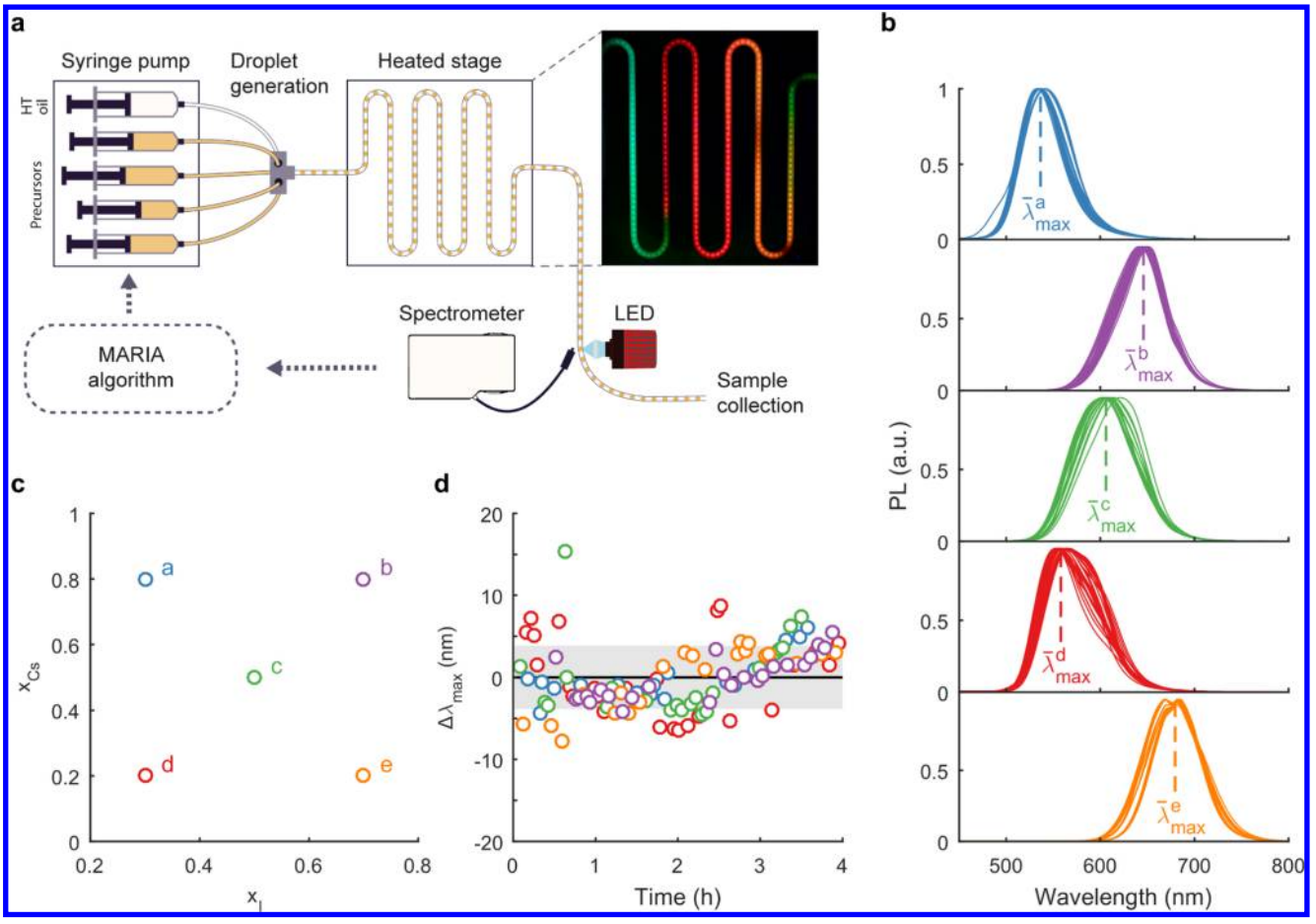

Figure 3. (a) Schematic of the experimental setup for the synthesis of $(Cs/FA)Pb(Br/I)_3$ NCs. The adaptive sampling algorithm iteratively adjusts the experimental conditions to drive the product nanocrystals toward a target emission wavelength based on spectroscopic measurements recorded thus far. The photograph shows a stream of droplets containing the reaction mixture under UV exposure and after a change in halide ratio. (b) Experimental error is evaluated by randomly performing experiments at one of five selected reaction conditions (a–e) with Cs doping and halide ratio defined in (c). The mean emission peak wavelength, $\bar{\lambda}^i_{max}$, is calculated from the spectra at each experimental condition and used to compute $\Delta\lambda_{max} = \lambda^i_{max} - \bar{\lambda}^i_{max}$. (d) Standard deviation of $\Delta\lambda_{max}$ (gray area) corresponds to the experimental error of our system, limiting the accuracy of synthesized nanomaterials PL peak wavelength to ±4 nm.

the mean and variance of the distribution of residuals: $Q_1 = \frac{1}{n}\sum_{i=1}^{n} E_i$ and $Q_2 = \frac{1}{n}\sum_{i=1}^{n} E_i^2$.[51,68] Ideally, the cross-validated residuals are consistent with the stochastic output of the BLUP, i.e., normally distributed around the predictor $\hat{y}$ with variance $\hat{s}^2$, with the moments taking values of $Q_1 = 0$ and $Q_2 = 1$.

RESULTS AND DISCUSSION

We allow MARIA to conduct experiments in an automatic and independent fashion by interfacing the algorithm with an automated microfluidic platform equipped with an online fluorescence detector (see the Supporting Information for details).[48] Segmented-flow capillary reactors provide an ideal platform for the high-throughput synthesis of $(Cs/FA)Pb(Br/I)_3$ nanocrystals, with real-time acquisition of PL spectra enabling fully automated operation (Figure S1).[26,28,53] A schematic representation of the setup is depicted in Figure 3a. Specifically, we achieve full control of caesium doping and halide ratio by blending four precursor solutions containing FA, FA + Cs, $PbBr_2$, and PbI_2. The combined flow rates remain pairwise constant according to $F_{FA} + F_{FA+Cs} = 2(F_{PbBr_2} + F_{PbI_2}) =$ constant, thus ensuring preservation of fixed concentrations of FA and Pb throughout.

To aid assessment of the error returned by the Kriging model, we evaluate the experimental error of our system. We do not expect a significant systematic error because the PL peak position of product particles shifts less than 4 nm over more than 180 min of continuous production (Figure S2). To assess reproducibility, we record spectra over the course of several hours, randomly switching experimental conditions within a set of five predetermined combinations of precursor flow rates (Figure 3b,c). For each set, we display deviations $\Delta\lambda_{max}$ from the average PL peak maximum $\bar{\lambda}_{max}$ ($\Delta\lambda_{max} = \lambda_{max} - \bar{\lambda}_{max}$) over time (Figure 3d). The errors are homogenously distributed throughout the parameter space with a standard deviation of ±4 nm, including errors introduced by the limited accuracy of syringe pumps and temperature controller, spectrometer resolution, and degradation of the precursor solutions over extended periods of time.

We first focus our attention on the synthesis of $(Cs/FA)Pb(Br/I)_3$ with controlled emission. Synthesis of formamidinium-based perovskite NCs requires an excess of FA over Pb, which we hold constant at [FA]/[Pb] = 8.[26] Reactions are performed at 120 °C to ensure the formation of nearly

DOI: 10.1021/acsami.8b03381
ACS Appl. Mater. Interfaces 2018, 10, 18869–18878

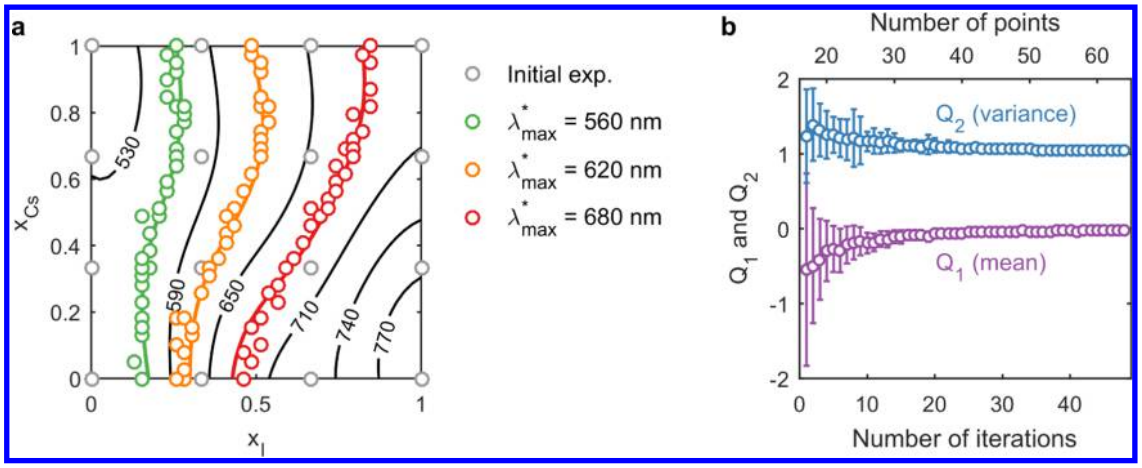

Figure 4. (a) Two-dimensional adaptive sampling experiment for the synthesis of (Cs/FA)Pb(Br/I)$_3$ NCs with targeted emission wavelengths, λ^*_{max}, of 560, 620, and 680 nm. Starting from a set of initial measurements (gray points), reaction conditions are iteratively selected by varying Cs doping (x_{Cs}) and halide ratio (x_I) based on a Kriging model (solid contour lines). (b) First and second moments (Q_1 and Q_2) of standardized residuals obtained by leave-one-out cross-validation. Sets of measurements with increasing length are randomly selected 30 times in a row to yield a distribution independent of the sampling sequence. A robust model, i.e., when Q_1 and Q_2 consistently take values of 0 and 1, respectively, is reached after approximately 20 iterations.

monodisperse cubic nanocrystals (Figure S3). Compositional tuning is achieved by varying the Cs concentration and halide ratio, forming a two-dimensional parameter space. The parameter $x_{Cs} = \frac{F_{FA}}{F_{FA} + F_{FA+Cs}}$ parametrizes Cs doping, with values ranging from 0 for [Cs]/[Pb] = 0 to 1 for [Cs]/[Pb] = 1.6. In addition, x_I corresponds to the iodide ratio defined as $x_I = \frac{[I]}{[I] + [Br]} = \frac{F_{PbBr_2}}{F_{PbBr_2} + F_{PbI_2}}$. It should also be noted that concentrations are related to the precursor solutions and generally do not correspond directly to crystal composition.[25] In a multidimensional parameter space, there may exist an infinite number of combinations yielding a specific PL peak wavelength and thus we avoid the stalling of the algorithm search by adding an extra constraint that forces the algorithm to select unvisited positions for a subsequent measurement. Initial measurement points lie on a homogeneous 4 × 4 grid distributed over the entire parameter space, which is discretized as a 40 × 40 grid corresponding to a resolution of about 0.5 μL/min with respect to precursor flow rates. As a rule of thumb, about 10d initial points are required for a first evaluation of the model in d dimensions.[60]

To illustrate our method, we identify reaction conditions that produce (Cs/FA)Pb(I/Br)$_3$ nanocrystals with target wavelengths of 560, 620, and 680 nm (Figure 4a). Starting from a set of initial measurements (gray points), MARIA iteratively selects subsequent measurement conditions that have the highest likelihood of reaching a target wavelength (colored points). Figure 4b illustrates the evolution of statistical indicators Q_1 and Q_2 (defined above) for an increasing number of iterations. Sets of points obtained through MARIA with increasing lengths are randomly selected to assess the quality of the model independent of the sampling sequence. At first, with very few points, residuals exhibit negative bias ($Q_1 < 0$) with a variance larger than predicted by the model ($Q_2 > 1$), indicating a highly sensitive response surface that is likely not representative of the experimental system. The addition of more points in the region of interest produces a more reliable model with cross-validated residuals in good agreement with the Kriging model predictions ($Q_1 \to 0$, $Q_2 \to 1$). In this example, approximately 20 iterations are required to generate a robust response surface, corresponding to 36 measurements (including initial samples). Importantly, systematic screening cannot reach a comparable model robustness in the region of interest with so few measurements (Figures 5 and S4). MARIA focuses on a region of interest to achieve a specific goal and perform experiments exclusively in the proximity of a target output. That said, systematic screening would provide a better overview of the entire parameter space than a target-oriented approach and would thus be desirable if the goal was to investigate the general functional dependence of optical properties on reaction conditions.[51]

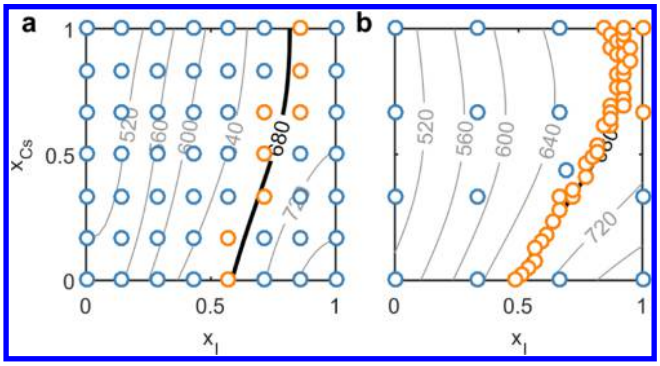

Figure 5. Systematic screening (a) compared with the MARIA procedure (b) after the same number of measurements (56 points) for a target PL peak wavelength of 680 nm. Orange data points are measurements where the PL emission is within our region of interest, i.e., 660−700 nm. Standardized cross-validated residuals of these points are characterized by $Q_1 = -0.17$ and $Q_2 = 1.8$ for (a) and $Q_1 = 0.06$ and $Q_2 = 1.0$ for (b) (see Figure S4 for the corresponding q−q plots). Even though the contour lines of the two resulting models exhibit similarities, the model obtained with MARIA is less sensitive and more representative of the experimental results.

We evaluate the accuracy of the final model returned by MARIA by performing measurements at the conditions predicted to result in a PL peak of 680 nm. We define a spatially weighted and normalized parameter ξ that follows the predicted line and increases according to $d\xi = \sqrt{dx_{Cs}^2 + dx_I^2}$, starting from $\xi = 0$ at $x_{Cs} = 0$ to $\xi = 1$ at $x_{Cs} = 1$ (Figure 6a).

DOI: 10.1021/acsami.8b03381
ACS Appl. Mater. Interfaces 2018, 10, 18869−18878

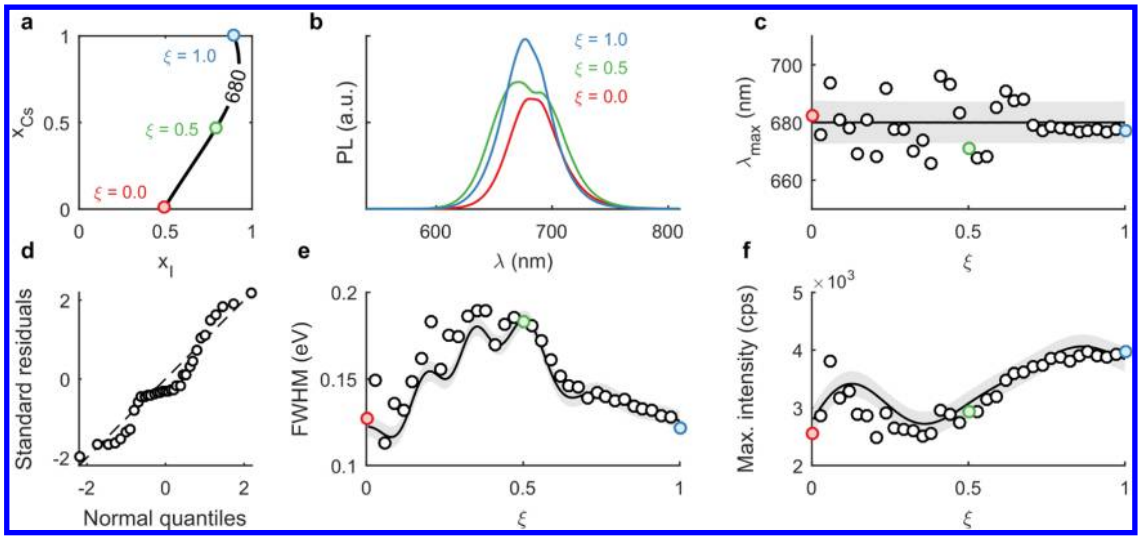

Figure 6. Validation of the model returned by MARIA for a targeted emission peak wavelength of 680 nm. (a) Spatial coordinate ξ is defined along the line of interest. (b) Experiments are systematically performed under the reaction conditions predicted by the model, and the corresponding spectra are recorded. (c) Measured PL peak wavelengths, λ_{max}, are compared with the model predictor (solid line) and its associated error (gray area). (d) Standardized residuals are computed and represented in a $q-q$ plot against normal quantiles. The model is used to predict other spectral properties such as FWHM (e) and maximum intensity (f) under the conditions with predicted emission at 680 nm.

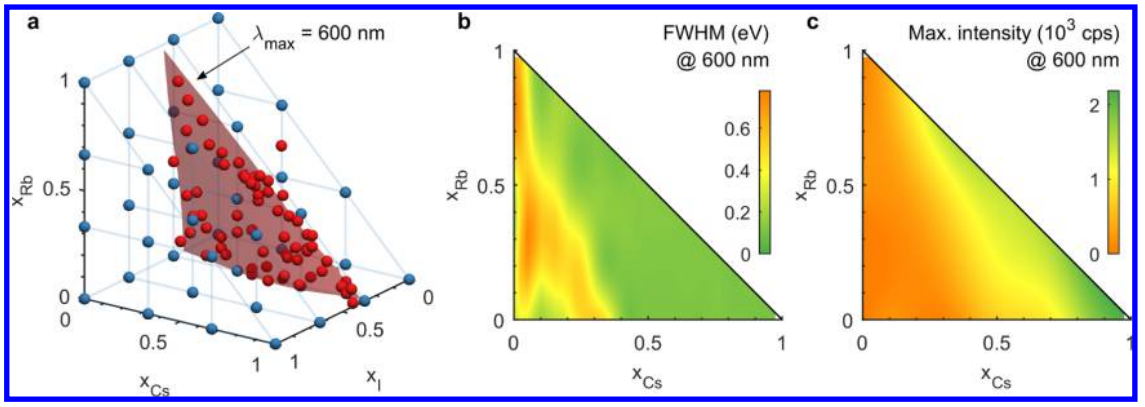

Figure 7. Adaptive sampling experiment for the synthesis of $(Rb/Cs/FA)Pb(Br/I)_3$ NCs in a three-dimensional parametric space with varying Cs doping (x_{Cs}), Rb doping (x_{Rb}), and halide ratio (x_I) and for a targeted emission wavelength of 600 nm. (a) Starting from a set of 40 initial measurements (blue spheres), MARIA selects conditions (red spheres) along the predicted 600 nm isosurface (transparent red surface). FWHM (b) and maximum intensity (c) of NCs are predicted under the reaction conditions predicted by the isosurface (projections on the $x_{Cs}-x_{Rb}$ plane are represented for clarity).

Forty measurements are performed for increasing values of ξ and compared with the Kriging predictions (Figure 6b,c). A $q-q$ plot of the residuals against normal quantiles confirms the excellent predictive ability of the final model (Figure 6d). Significantly, this implies that the model error is intrinsically consisted of the error linked to the interpolation and sampling (as determined in Figure 3d) without a priori inputs from the user. The model also serves as a platform to compare NCs with similar PL emission, as it is able to predict other spectral properties, such as FWHM (Figure 6e) and maximum intensity (Figure 6f). Indeed, we find that low and mid levels of Cs doping are detrimental to PL intensities and produce broader emission peaks, possibly due to the higher Br content required to compensate the blue shift caused by caesium and reach the targeted emission peak wavelength of 680 nm.[26] Conversely, high Cs concentrations produce NCs exhibiting higher intensities and narrower emission peaks.

In light of the superior optical performance of multinary LHP systems detailed in the introduction, we extend the procedure to a three-dimensional chemical system for the synthesis of $(Cs/Rb/FA)Pb(Br/I)_3$ NCs with a target PL peak at 600 nm. We include an extra parameter x_{Rb}, directly proportional to the Rb doping concentration, increasing from $x_{Rb} = 0$ at [Rb] = 0 to $x_{Rb} = 1$ at [Rb]/[Pb] = 1.6. Figure 7a displays the data with the 600 nm surface obtained by MARIA in a three-dimensional parameter space formed by x_I, x_{Cs}, and x_{Rb}. Starting from 40 initial measurements spread on a truncated $4 \times 4 \times 4$ grid (blue spheres), MARIA performs 60 measurements (red spheres) to generate an insensitive and reliable model (Figure S5). The entire procedure takes approximately 3 h to complete and uses less than 50 mL of precursor solutions (<75 mg of lead). Figure 7b,c shows the values of FWHM and maximum intensity on the 600 nm isosurface. With its small ionic radius, Rb^+ is not easily incorporated into the perovskite lattice, resulting in a small influence on the PL peak wavelength and broadening.[69] However, it has been shown to have a significant impact on stability, forming a photoinactive phase that acts as a protective

DOI: 10.1021/acsami.8b03381
ACS Appl. Mater. Interfaces 2018, 10, 18869−18878

layer.[70] We also note that doping with Cs^+ is essential to ensure high PL intensities and reportedly increases the phase stability of FA-based LHPs.[67] On the basis of these considerations and the model outputs, we are able to select several promising reaction conditions for further investigation in the form of QY measurements or studies on long-term photostability. In the current study, we would, for example, focus our attention on various points along the diagonal (i.e., [Rb] + [Cs] = 1.6[Pb] up to [Rb] ≤ 1.2[Pb] with halide ratios predicted by the 600 nm isosurface), which exhibit narrower PL peaks and higher intensities when compared with the undoped NC composition.

CONCLUSIONS

We have successfully developed a high-throughput microfluidic platform for the rapid and automated identification of reagent concentrations that yield NCs with defined emission properties. An adaptive sampling algorithm based on a Kriging regression model computes a response surface based on spectroscopic measurements under previously visited experimental conditions and selects subsequent optimal sampling points with the highest likelihood of reaching a target PL peak wavelength. Importantly, the novel goal-seeking approach developed herein is straightforwardly compared with methods based on objective functions and is, in addition, computationally undemanding. The application of MARIA to the synthesis of $(Cs/FA)Pb(Br/I)_3$ and $(Rb/Cs/FA)Pb(Br/I)_3$ NCs with various target emission wavelengths results in models that efficiently capture the experimental error and exhibit high accuracy after only a few dozen iterations. Moreover, the models also enable prediction of other observable spectral properties under the conditions of interest, thus providing a convenient basis for the selection of promising conditions to scale-up or for application-oriented performance and stability tests, in particular concerning stability, which remains a key challenge for the successful implementation of LHP materials in display applications. Stability tests represent a time-consuming task and should be performed on a minimal number of carefully selected material candidates.

EXPERIMENTAL SECTION

Chemicals. 1-Octadecene (ODE, 90%), oleic acid (OA, 90%), toluene (99.8%), butyl acetate (BuOAc, >99%), formamidine acetate (FAOAc, 99%), lead(II) bromide ($PbBr_2$, >98%), and cesium carbonate (Cs_2CO_3, 99.9%) were purchased from Sigma-Aldrich. Oleyl amine (OLA, 80−90%) and lead(II) iodide (PbI_2, >99.999%) were ordered from Acros Organics and Strem, respectively. All chemicals were used as received without further purifications.

Precursor Preparation. Two separate precursor solutions containing lead bromide and lead iodide are prepared to reach full control over halide ratios. Additional precursor solutions contain formamidinium and, optionally, a high concentration of Cs or Rb (one solution with pure formamidinium and one solution for each type of dopant, keeping the concentration of formamidinium constant throughout).

Lead Halide Precursor. $PbBr_2$ (62 mg, 0.17 mmol, 1 equiv) or PbI_2 (77 mg, 0.17 mmol, 1 equiv) is suspended in 8.5 mL of ODE in a 20 mL Schlenk flask. The mixture is degassed for 1 h at 130 °C and subsequently degassed OA (1 mL) and degassed OLA (0.5 mL) are added under a N_2 atmosphere. The solution is stirred until clear, removed from heat, and left to cool to RT while stirring is continued.

Formamidinium Oleate Precursor. A 20 mL Schlenk flask is charged with 70 mg of FAOAc (0.67 mmol, 4 equiv), 8 mL of ODE, and 2 mL of OA. Depending on the experiment, 22 mg of Cs_2CO_3 (0.07 mmol, 0.4 equiv) or 16 mg of Rb_2CO_3 (0.07 mmol, 0.4 equiv) is added to the mixture. The suspension is degassed at RT for 30 min under vacuum and subsequently heated to 120 °C under a nitrogen atmosphere for 20 min. After complete dissolution has taken place, the resulting solution is quickly cooled to RT with a water bath.

Microfluidic Reactor Setup. Precursor solutions and perfluorinated heat transfer oil (Galden HT 270, Solvay) are loaded in glass syringes (Gastight 1000, Hamilton, Switzerland) and operated using a Nemesys syringe pump (Cetoni, Germany). The syringes are connected with FEP (01/16″ OD, 700 μm ID, IDEX Health & Science) to a 7-port manifold (PEEK, 0.5 mm thru-hole, IDEX Health & Science) that generates a stream of isolate microdroplets with volumes of 0.5−1.5 μL. The segmented flow enters a PTFE capillary (01/16″ OD, 500 μm ID, AdTech, U.K.), which meanders through an aluminum heating zone that can be maintained at temperatures up to 180 °C with a ceramic heater (Ultramic, Watlow). After leaving the reactor, the droplets are transferred to a high-purity PFA capillary (1/16″ OD, 500 μm ID), where fluorescence spectra are recorded with a 365 nm mounted LED (190 mW, Thorlabs) as the excitation light source and an optical fiber in orthogonal configuration connected to a CCD spectrometer (QE65 Pro, Ocean Optics).

An in-house-developed LabVIEW program (LabVIEW 2016) adjusts the heating power to maintain the temperature of the reactor within ±0.5 K of the set value. The LabVIEW script (Figure S1) accepts a list of experimental parameters and automatically measures the corresponding fluorescence spectra by adapting the relative flow rates, residence time, and temperature. An adaptive sampling algorithm is implemented in MATLAB 2016a and is iteratively called within the LabVIEW script.

ASSOCIATED CONTENT

Supporting Information

The Supporting Information is available free of charge on the ACS Publications website at DOI: 10.1021/acsami.8b03381.

Model derivation, method flowchart and reactor stability, particle size distribution, and model validation in two-dimensional and three-dimensional (PDF)

AUTHOR INFORMATION

Corresponding Authors

*E-mail: mvkovalenko@ethz.ch (M.V.K.).
*E-mail: andrew.demello@chem.ethz.ch (A.J.M.).

ORCID

Leonard Bezinge: 0000-0002-9733-9697
Richard M. Maceiczyk: 0000-0001-5735-2689
Ioannis Lignos: 0000-0002-6816-3290
Maksym V. Kovalenko: 0000-0002-6396-8938
Andrew J. deMello: 0000-0003-1943-1356

Notes

The authors declare no competing financial interest.

ACKNOWLEDGMENTS

The authors would like to thank Franziska Krieg for the acquisition of TEM micrographs. AdM acknowledges partial support from a National Research Foundation (NRF) grant funded by the Ministry of Science, ICT and Future Planning of Korea, through the Global Research Laboratory Program (Grant number 2009-00426).

REFERENCES

(1) Schmidt, L. C.; Pertegás, A.; González-Carrero, S.; Malinkiewicz, O.; Agouram, S.; Mínguez Espallargas, G.; Bolink, H. J.; Galian, R. E.; Pérez-Prieto, J. Nontemplate Synthesis of CH3NH3PbBr3 Perovskite Nanoparticles. *J. Am. Chem. Soc.* **2014**, *136*, 850−853.

(2) Protesescu, L.; Yakunin, S.; Bodnarchuk, M. I.; Krieg, F.; Caputo, R.; Hendon, C. H.; Yang, R. X.; Walsh, A.; Kovalenko, M. V.

DOI: 10.1021/acsami.8b03381
ACS Appl. Mater. Interfaces 2018, 10, 18869−18878

Nanocrystals of Cesium Lead Halide Perovskites (CsPbX3, X = Cl, Br, and I): Novel Optoelectronic Materials Showing Bright Emission with Wide Color Gamut. *Nano Lett.* **2015**, *15*, 3692−3696.
(3) Huang, H.; Polavarapu, L.; Sichert, J. A.; Susha, A. S.; Urban, A. S.; Rogach, A. L. Colloidal Lead Halide Perovskite Nanocrystals: Synthesis, Optical Properties and Applications. *NPG Asia Mater.* **2016**, *8*, No. e328.
(4) Huang, H.; Bodnarchuk, M.; Kershaw, S. V.; Kovalenko, M. V.; Rogach, A. L. Lead Halide Perovskite Nanocrystals in the Research Spotlight: Stability and Defect-Tolerance. *ACS Energy Lett.* **2017**, *2*, 2071−2083.
(5) Kovalenko, M. V.; Protesescu, L.; Bodnarchuk, M. I. Properties and Potential Optoelectronic Applications of Lead Halide Perovskite Nanocrystals. *Science* **2017**, *358*, 745−750.
(6) Wang, Y.; Li, X.; Song, J.; Xiao, L.; Zeng, H.; Sun, H. All-Inorganic Colloidal Perovskite Quantum Dots: A New Class of Lasing Materials with Favorable Characteristics. *Adv. Mater.* **2015**, *27*, 7101−7108.
(7) Yakunin, S.; Protesescu, L.; Krieg, F.; Bodnarchuk, M. I.; Nedelcu, G.; Humer, M.; De Luca, G.; Fiebig, M.; Heiss, W.; Kovalenko, M. V. Low-Threshold Amplified Spontaneous Emission and Lasing from Colloidal Nanocrystals of Caesium Lead Halide Perovskites. *Nat. Commun.* **2015**, *6*, No. 8515.
(8) Pan, J.; Sarmah, S. P.; Murali, B.; Dursun, I.; Peng, W.; Parida, M. R.; Liu, J.; Sinatra, L.; Alyami, N.; Zhao, C.; Alarousu, E.; Ng, T. K.; Ooi, B. S.; Bakr, O. M.; Mohammed, O. F. Air-Stable Surface-Passivated Perovskite Quantum Dots for Ultra-Robust, Single- and Two-Photon-Induced Amplified Spontaneous Emission. *J. Phys. Chem. Lett.* **2015**, *6*, 5027−5033.
(9) Wang, Y.; Li, X.; Zhao, X.; Xiao, L.; Zeng, H.; Sun, H. Nonlinear Absorption and Low-Threshold Multiphoton Pumped Stimulated Emission from All-Inorganic Perovskite Nanocrystals. *Nano Lett.* **2016**, *16*, 448−453.
(10) Zhang, F.; Zhong, H.; Chen, C.; Wu, X.; Hu, X.; Huang, H.; et al. Brightly Luminescent and Color- (X = Br, I, Cl) Quantum Dots: Potential Alternatives for Display Technology. *ACS Nano* **2015**, *3*, 4533−4542.
(11) Zhang, X.; Liu, H.; Wang, W.; Zhang, J.; Xu, B.; Karen, K. L.; Zheng, Y.; Liu, S.; Chen, S.; Wang, K.; Sun, X. W. Hybrid Perovskite Light-Emitting Diodes Based on Perovskite Nanocrystals with Organic−Inorganic Mixed Cations. *Adv. Mater.* **2017**, *29*, 1−7.
(12) Song, J.; Li, J.; Li, X.; Xu, L.; Dong, Y.; Zeng, H. Quantum Dot Light-Emitting Diodes Based on Inorganic Perovskite Cesium Lead Halides (CsPbX3). *Adv. Mater.* **2015**, *27*, 7162−7167.
(13) Li, X.; Wu, Y.; Zhang, S.; Cai, B.; Gu, Y.; Song, J.; Zeng, H. CsPbX3 Quantum Dots for Lighting and Displays: Roomerature Synthesis, Photoluminescence Superiorities, Underlying Origins and White Light-Emitting Diodes. *Adv. Funct. Mater.* **2016**, *26*, 2435−2445.
(14) Tan, Y.; Zou, Y.; Wu, L.; Huang, Q.; Yang, D.; Chen, M.; Ban, M.; Wu, C.; Wu, T.; Bai, S.; Song, T.; Zhang, Q.; Sun, B. Highly Luminescent and Stable Perovskite Nanocrystals with Octylphosphonic Acid as Ligand for Efficient Light Emitting Diodes. *ACS Appl. Mater. Interfaces* **2018**, *10*, 3784−3792.
(15) Park, Y. S.; Guo, S.; Makarov, N. S.; Klimov, V. I. Room Temperature Single-Photon Emission from Individual Perovskite Quantum Dots. *ACS Nano* **2015**, *9*, 10386−10393.
(16) Rainò, G.; Nedelcu, G.; Protesescu, L.; Bodnarchuk, M. I.; Kovalenko, M. V.; Mahrt, R. F.; Stöferle, T. Single Cesium Lead Halide Perovskite Nanocrystals at Low Temperature: Fast Single-Photon Emission, Reduced Blinking, and Exciton Fine Structure. *ACS Nano* **2016**, *10*, 2485−2490.
(17) Kojima, A.; Teshima, K.; Shirai, Y.; Miyasaka, T. Organometal Halide Perovskites as Visible-Light Sensitizers for Photovoltaic Cells. *J. Am. Chem. Soc.* **2009**, *131*, 6050−6051.
(18) Im, J.-H.; Lee, C.-R.; Lee, J.-W.; Park, S.-W.; Park, N.-G. 6.5% Efficient Perovskite Quantum-Dot-Sensitized Solar Cell. *Nanoscale* **2011**, *3*, 4088.
(19) Swarnkar, A.; Marshall, A. R.; Sanehira, E. M.; Chernomordik, B. D.; Moore, D. T.; Christians, J. A.; Chakrabarti, T.; Luther, J. M. Quantum Dot-Induced Phase Stabilization of -CsPbI3 Perovskite for High-Efficiency Photovoltaics. *Science* **2016**, *354*, 92−95.
(20) Mali, S. S.; Shim, C. S.; Hong, C. K. Highly Stable and Efficient Solid-State Solar Cells Based on Methylammonium Lead Bromide (CH3NH3PbBr3) Perovskite Quantum Dots. *NPG Asia Mater.* **2015**, *7*, No. e208.
(21) Ramasamy, P.; Lim, D.-H.; Kim, B.; Lee, S.-H.; Lee, M.-S.; Lee, J.-S. All-Inorganic Cesium Lead Halide Perovskite Nanocrystals for Photodetector Applications. *Chem. Commun.* **2016**, *52*, 2067−2070.
(22) Gonzalez-Carrero, S.; Francès-Soriano, L.; González-Béjar, M.; Agouram, S.; Galian, R. E.; Pérez-Prieto, J. The Luminescence of CH3NH3PbBr3 Perovskite Nanoparticles Crests the Summit and Their Photostability under Wet Conditions Is Enhanced. *Small* **2016**, 5245−5250.
(23) Protesescu, L.; Yakunin, S.; Bodnarchuk, M. I.; Bertolotti, F.; Masciocchi, N.; Guagliardi, A.; Kovalenko, M. V. Monodisperse Formamidinium Lead Bromide Nanocrystals with Bright and Stable Green Photoluminescence. *J. Am. Chem. Soc.* **2016**, *138*, 14202−14205.
(24) Levchuk, I.; Osvet, A.; Tang, X.; Brandl, M.; Perea, J. D.; Hoegl, F.; Matt, G. J.; Hock, R.; Batentschuk, M.; Brabec, C. J. Brightly Luminescent and Color-Tunable Formamidinium Lead Halide Perovskite FAPbX3 (X = Cl, Br, I) Colloidal Nanocrystals. *Nano Lett.* **2017**, *17*, 2765−2770.
(25) Protesescu, L.; Yakunin, S.; Kumar, S.; Bär, J.; Bertolotti, F.; Masciocchi, N.; Guagliardi, A.; Grotevent, M.; Shorubalko, I.; Bodnarchuk, M. I.; Shih, C. J.; Kovalenko, M. V. Dismantling The "red Wall" of Colloidal Perovskites: Highly Luminescent Formamidinium and Formamidinium-Cesium Lead Iodide Nanocrystals. *ACS Nano* **2017**, *11*, 3119−3134.
(26) Maceiczyk, R. M.; Dümbgen, K.; Lignos, I.; Protesescu, L.; Kovalenko, M. V.; Demello, A. J. Microfluidic Reactors Provide Preparative and Mechanistic Insights into the Synthesis of Formamidinium Lead Halide Perovskite Nanocrystals. *Chem. Mater.* **2017**, *29*, 8433−8439.
(27) Lignos, I.; Protesescu, L.; Emiroglu, D. B.; Maceiczyk, R. M.; Schneider, S.; Kovalenko, M. V.; DeMello, A. J. Unveiling the Shape Evolution and Halide-Ion-Segregation in Blue Emitting Formamidinium Lead Halide Perovskite Nanocrystals Using an Automated Microfluidic Platform. *Nano Lett.* **2018**, *18*, 1246−1252.
(28) Lignos, I.; Stavrakis, S.; Nedelcu, G.; Protesescu, L.; Demello, A. J.; Kovalenko, M. V. Synthesis of Cesium Lead Halide Perovskite Nanocrystals in a Droplet-Based Microfluidic Platform: Fast Parametric Space Mapping. *Nano Lett.* **2016**, *16*, 1869−1877.
(29) Swarnkar, A.; Chulliyil, R.; Ravi, V. K.; Irfanullah, M.; Chowdhury, A.; Nag, A. Colloidal CsPbBr3 Perovskite Nanocrystals: Luminescence beyond Traditional Quantum Dots. *Angew. Chem., Int. Ed.* **2015**, *54*, 15424−15428.
(30) Krieg, F.; Ochsenbein, S.; Yakunin, S.; ten Brinck, S.; Aellen, P.; Süess, A.; Clerc, B.; Guggisberg, D.; Nazarenko, O.; Shynkarenko, Y.; Kumar, S.; Shih, C.-J.; Infante, I.; Kovalenko, M. V. Colloidal CsPbX3 (X = Cl, Br, I) Nanocrystals 2.0: Zwitterionic Capping Ligands for Improved Durability and Stability. *ACS Energy Lett.* **2018**, 641−646.
(31) Van der Stam, W.; Geuchies, J. J.; Altantzis, T.; Van Den Bos, K. H. W.; Meeldijk, J. D.; Van Aert, S.; Bals, S.; Vanmaekelbergh, D.; De Mello Donega, C. Highly Emissive Divalent-Ion-Doped Colloidal CsPb1-xMxBr3 Perovskite Nanocrystals through Cation Exchange. *J. Am. Chem. Soc.* **2017**, *139*, 4087−4097.
(32) Liu, H.; Wu, Z.; Shao, J.; Yao, D.; Gao, H.; Liu, Y.; Yu, W.; Zhang, H.; Yang, B. CsPbxMn1-xCl3 Perovskite Quantum Dots with High Mn Substitution Ratio. *ACS Nano* **2017**, *11*, 2239−2247.
(33) Parobek, D.; Roman, B. J.; Dong, Y.; Jin, H.; Lee, E.; Sheldon, M.; Son, D. H. Exciton-to-Dopant Energy Transfer in Mn-Doped Cesium Lead Halide Perovskite Nanocrystals. *Nano Lett.* **2016**, *16*, 7376−7380.
(34) Begum, R.; Parida, M. R.; Abdelhady, A. L.; Murali, B.; Alyami, N. M.; Ahmed, G. H.; Hedhili, M. N.; Bakr, O. M.; Mohammed, O. F.

DOI: 10.1021/acsami.8b03381
ACS Appl. Mater. Interfaces 2018, 10, 18869−18878

Engineering Interfacial Charge Transfer in CsPbBr3 Perovskite Nanocrystals by Heterovalent Doping. *J. Am. Chem. Soc.* **2017**, *139*, 731−737.
(35) Guria, A. K.; Dutta, S. K.; Adhikari, S. D.; Pradhan, N. Doping Mn2+ in Lead Halide Perovskite Nanocrystals: Successes and Challenges. *ACS Energy Lett.* **2017**, *2*, 1014−1021.
(36) Syzgantseva, O. A.; Saliba, M.; Graetzel, M.; Rothlisberger, U. Stabilization of the Perovskite Phase of Formamidinium Lead Triiodide by Methylammonium, Cs, And/or Rb Doping. *J. Phys. Chem. Lett.* **2017**, *8*, 1191−1196.
(37) Saliba, M.; Matsui, T.; Domanski, K.; Seo, J.-Y.; Ummadisingu, A.; Zakeeruddin, S. M.; Correa-Baena, J.-P.; Tress, W. R.; Abate, A.; Hagfeldt, A.; Gratzel, M. Incorporation of Rubidium Cations into Perovskite Solar Cells Improves Photovoltaic Performance. *Science* **2016**, *354*, 206−209.
(38) Saliba, M.; Matsui, T.; Seo, J.-Y.; Domanski, K.; Correa-Baena, J.-P.; Nazeeruddin, M. K.; Zakeeruddin, S. M.; Tress, W.; Abate, A.; Hagfeldt, A.; Grätzel, M. Cesium-Containing Triple Cation Perovskite Solar Cells: Improved Stability, Reproducibility and High Efficiency. *Energy Environ. Sci.* **2016**, *9*, 1989−1997.
(39) Park, Y. H.; Jeong, I.; Bae, S.; Son, H. J.; Lee, P.; Lee, J.; Lee, C. H.; Ko, M. J. Inorganic Rubidium Cation as an Enhancer for Photovoltaic Performance and Moisture Stability of HC(NH2)2PbI3 Perovskite Solar Cells. *Adv. Funct. Mater.* **2017**, *27*, 21−27.
(40) Goldschmidt, V. M. Die Gesetze Der Krystallochemie. *Naturwissenschaften* **1926**, *14*, 477−485.
(41) Travis, W.; Glover, E. N. K.; Bronstein, H.; Scanlon, D. O.; Palgrave, R. G. On the Application of the Tolerance Factor to Inorganic and Hybrid Halide Perovskites: A Revised System. *Chem. Sci.* **2016**, *7*, 4548−4556.
(42) Kieslich, G.; Sun, S.; Cheetham, A. K. Solid-State Principles Applied to Organic−inorganic Perovskites: New Tricks for an Old Dog. *Chem. Sci.* **2014**, *5*, 4712−4715.
(43) Filip, M. R.; Eperon, G. E.; Snaith, H. J.; Giustino, F. Steric Engineering of Metal-Halide Perovskites with Tunable Optical Band Gaps. *Nat. Commun.* **2014**, *5*, No. 5757.
(44) Sun, S.; Yuan, D.; Xu, Y.; Wang, A.; Deng, Z. Ligand-Mediated Synthesis of Shape-Controlled Cesium Lead Halide Perovskite Nanocrystals via Reprecipitation Process at Room Temperature. *ACS Nano* **2016**, *10*, 3648−3657.
(45) Chiu, D. T.; deMello, A. J.; Di Carlo, D.; Doyle, P. S.; Hansen, C.; Maceiczyk, R. M.; Wootton, R. C. R. Small but Perfectly Formed? Successes, Challenges, and Opportunities for Microfluidics in the Chemical and Biological Sciences. *Chem* **2017**, *2*, 201−223.
(46) Phillips, T. W.; Lignos, I. G.; Maceiczyk, R. M.; deMello, A. J.; deMello, J. C. Nanocrystal Synthesis in Microfluidic Reactors: Where Next? *Lab Chip* **2014**, *14*, 3172.
(47) Lignos, I.; Maceiczyk, R.; DeMello, A. J. Microfluidic Technology: Uncovering the Mechanisms of Nanocrystal Nucleation and Growth. *Acc. Chem. Res.* **2017**, *50*, 1248−1257.
(48) Maceiczyk, R. M.; Lignos, I. G.; Demello, A. J. Online Detection and Automation Methods in Microfluidic Nanomaterial Synthesis. *Curr. Opin. Chem. Eng.* **2015**, *8*, 29−35.
(49) Edel, J. B.; Fortt, R.; deMello, J. C.; deMello, A. J. Microfluidic Routes to the Controlled Production of Nanoparticles. *Chem. Commun.* **2002**, 1136−1137.
(50) Nightingale, A. M.; deMello, J. C. Segmented Flow Reactors for Nanocrystal Synthesis. *Adv. Mater.* **2013**, *25*, 1813−1821.
(51) Maceiczyk, R. M.; DeMello, A. J. Fast and Reliable Metamodeling of Complex Reaction Spaces Using Universal Kriging. *J. Phys. Chem. C* **2014**, *118*, 20026−20033.
(52) Maceiczyk, R. M.; Bezinge, L.; deMello, A. J. Kinetics of Nanocrystal Synthesis in a Microfluidic Reactor: Theory and Experiment. *React. Chem. Eng.* **2016**, *1*, 261−271.
(53) Epps, R. W.; Felton, K. C.; Coley, C. W.; Abolhasani, M. Automated Microfluidic Platform for Systematic Studies of Colloidal Perovskite Nanocrystals: Towards Continuous Nano-Manufacturing. *Lab Chip* **2017**, *17*, 4040−4047.
(54) Reizman, B. J.; Jensen, K. F. Feedback in Flow for Accelerated Reaction Development. *Acc. Chem. Res.* **2016**, *49*, 1786−1796.
(55) Krishnadasan, S.; Brown, R. J. C.; deMello, A. J.; deMello, J. C. Intelligent Routes to the Controlled Synthesis of Nanoparticles. *Lab Chip* **2007**, *7*, 1434.
(56) Moore, J. S.; Jensen, K. F. Automated Multitrajectory Method for Reaction Optimization in a Microfluidic System Using Online IR Analysis. *Org. Process Res. Dev.* **2012**, *16*, 1409−1415.
(57) McMullen, J. P.; Jensen, K. F. An Automated Microfluidic System for Online Optimization in Chemical Synthesis. *Org. Process Res. Dev.* **2010**, *14*, 1169−1176.
(58) Matheron, G. Principles of Geostatistics. *Econ. Geol.* **1963**, *58*, 1246−1266.
(59) Forrester, A. I. J.; Keane, A. J.; Bressloff, N. W. Design and Analysis of "Noisy" Computer Experiments. *AIAA J.* **2006**, *44*, 2331−2339.
(60) Jones, D. R.; Schonlau, M.; Welch, W. J. Efficient Global Optimization of Expensive Black-Box Functions. *J. Global Optim.* **1998**, *13*, 455−492.
(61) Jones, D. R. A Taxonomy of Global Optimization Methods Based on Response Surfaces. *J. Global Optim.* **2001**, *21*, 345−383.
(62) Forrester, A. I. J.; Keane, A. J. Recent Advances in Surrogate-Based Optimization. *Prog. Aeronaut. Sci.* **2009**, *45*, 50−79.
(63) Müller, D.; Dercks, B.; Nabati, E.; Blazek, M.; Eifert, T.; Schallenberg, J.; Piechottka, U.; Dadhe, K. Real-Time Optimization in the Chemical Processing Industry. *Chem. Ing. Tech.* **2017**, *89*, 1464−1470.
(64) Simpson, T. W.; Peplinski, J. D.; Koch, P. N.; Allen, J. K. Metamodels for Computer-Based Engineering Design: Survey and Recommendations. *Eng. Comput.* **2001**, *17*, 129−150.
(65) Sacks, J.; Welch, W. J.; Mitchell, T. J.; Wynn, H. P. Design and Analysis of Computer Experiments. *Stat. Sci.* **1989**, *4*, 409−423.
(66) Chan, E. M.; Xu, C.; Mao, A. W.; Han, G.; Owen, J. S.; Cohen, B. E.; Milliron, D. J. Reproducible, High-Throughput Synthesis of Colloidal Nanocrystals for Optimization in Multidimensional Parameter Space. *Nano Lett.* **2010**, *10*, 1874−1885.
(67) Li, Z.; Yang, M.; Park, J. S.; Wei, S. H.; Berry, J. J.; Zhu, K. Stabilizing Perovskite Structures by Tuning Tolerance Factor: Formation of Formamidinium and Cesium Lead Iodide Solid-State Alloys. *Chem. Mater.* **2016**, *28*, 284−292.
(68) Eberly, S.; Swall, J.; Holland, D.; Cox, B.; Baldridge, E. *Developing Spatially Interpolated Surfaces and Estimating Uncertainty*; U.S. Environmental Protection Agency, Office of Air and Radiation, Office of Air Quality Planning and Standards, 2004.
(69) Kubicki, D. J.; Prochowicz, D.; Hofstetter, A.; Zakeeruddin, S. M.; Grätzel, M.; Emsley, L. Phase Segregation in Cs-, Rb- and K-Doped Mixed-Cation (MA)x(FA)1−xPbI3 Hybrid Perovskites from Solid-State NMR. *J. Am. Chem. Soc.* **2017**, *139*, 14173−14180.
(70) Philippe, B.; Saliba, M.; Correa-Baena, J. P.; Cappel, U. B.; Turren-Cruz, S. H.; Grätzel, M.; Hagfeldt, A.; Rensmo, H. Chemical Distribution of Multiple Cation (Rb+, Cs+, MA+, and FA+) Perovskite Materials by Photoelectron Spectroscopy. *Chem. Mater.* **2017**, *29*, 3589−3596.

DOI: 10.1021/acsami.8b03381
ACS Appl. Mater. Interfaces 2018, 10, 18869−18878